To be published in Optica:

Title:	Engineering spatial coherence in lattices of polariton condensates
Authors:	Julian Toepfer,Ioannis Chatzopoulos,Helgi Sigurdsson,Tamsin Cookson,Yuri Rubo,Pavlos Lagoudakis
Accepted:	06 December 20
Posted	07 December 20
DOI:	https://doi.org/10.1364/OPTICA.409976

Engineering spatial coherence in lattices of polariton condensates

J. D. Töpfer[1,2], I. Chatzopoulos[1], H. Sigurdsson[1,2], T. Cookson[1], Y. G. Rubo[3], and P. G. Lagoudakis[1,2,*]

[1] School of Physics and Astronomy, University of Southampton, Southampton, SO17 1BJ, United Kingdom
[2] Skolkovo Institute of Science and Technology, Moscow, Bolshoy Boulevard 30, bld. 1, 121205, Russia
[3] Instituto de Energías Renovables, Universidad Nacional Autónoma de México, Temixco, Morelos, 62580, Mexico
[*] Corresponding author: P.Lagoudakis@skoltech.ru

Compiled November 29, 2020

Artificial lattices of coherently coupled macroscopic states are at the heart of applications ranging from solving hard combinatorial optimisation problems to simulating complex many-body physical systems. The size and complexity of the problems scales with the extent of coherence across the lattice. Although the fundamental limit of spatial coherence depends on the nature of the couplings and lattice parameters, it is usually engineering constrains that define the size of the system. Here, we engineer polariton condensate lattices with active control on the spatial arrangement and condensate density that result in near-diffraction limited emission, and spatial coherence that exceeds by nearly two orders of magnitude the size of each individual condensate. We utilise these advancements to unravel the dependence of spatial correlations between polariton condensates on the lattice geometry.

http://dx.doi.org/10.1364/ao.XX.XXXXXX

1. INTRODUCTION

Synchronisation and the emergence of coherence between coupled elements are universal concepts arising in nature and technology [1]. They dictate collective human behaviour [2], functioning of neurological systems [3], as well as phase transitions of quantum systems to macroscopically collective entities at low temperatures [4]. For small-size systems such as two mechanical pendulums coupled through a common support [5] or two coupled laser cavities [6] frequency locking of the two elements depends on the inter-element coupling strength in competition with any inherent dephasing mechanisms. In larger systems consisting of many interacting elements, such as social structures or coupled laser networks the underlying coupling topology (or network architecture) critically influences the dynamics and coherence formed in these systems [7, 8]. Engineering spatial coherence in such large networks is a key element for increasing system performances in power grids [9], novel computational devices for classification tasks [10] or laser arrays for creation and control of high power beams [11].

Lattices of coupled condensates are investigated for the simulation and computation of complex tasks in atomic [12–14], photonic [15] and polaritonic [16–18] platforms. Functionality and computational performance of these systems is ultimately limited by the system's spatial coherence length, i.e. how many condensates can coherently be coupled. From a more fundamental point of view, increasing the coherence allows one to construct a larger many-body system and approach the ideal limit of a homogeneous "infinite" order parameter, which is essential for the study of phase transitions in interacting bosonic systems such as the Berezinskii-Kosterlitz-Thouless transition in two-dimensions (2D) [19].

Macroscopically coherent systems of exciton-polaritons, hybrid light-matter quasiparticles [20], bring together the speed and optical control of photonic platforms and the nonlinearities found in strongly interacting matter systems. As such, polariton lattices offer an all-optical control over the reconfigurable non-Hermitian potential landscape and the in-plane particle current provided by optical imprinting of excitonic reservoirs [21–25]. In the case of polariton condensates in semiconductor microcavites, measurements were initially limited to small condensate sizes [26–29] but advancements in sample fabrication and experimental techniques now allow studies on their coherence properties as extended objects far away from the excitation area [21, 30], in optical traps [31, 32], and photonic microstructures [33]. The emergence of correlations beyond the spatial extension of the laser excitation area has underpinned the creation of networks and lattices of polariton condensates.

Here, we engineer control over the particle density and position of each polariton condensate across a polariton lattice under non-resonant optical excitation. We overcome the challenge of disorder induced localisation and dephasing by employing a feedback scheme for each individual laser spot, balancing the

condensate density and allowing us to accurately study the decay of coherence across different coupling topologies. The result is a homogeneous macroscopic, high energy, condensate lattice with coherence length exceeding multiple lattice cells and near-diffraction limited emission. Generating such large condensate lattices by using multiple excitation sources allows us to go beyond the standard single-excitation source limit [21, 30] overcoming beam size limitations, beam profile inhomogeneities, and condensate fragmentation [20]. We observe that the connectivity of the lattice significantly enhances the system's coherence length due to increased coherent coupling between adjacent condensates.

2. RESULTS

We optically generate lattices of coupled polariton condensates using non-resonant, pulsed and tightly-focused laser excitation spots for each condensate node (see Supplementary Section S1 for methods). Exemplary plots of optically engineered homogeneous lattices in square and triangular configuration are illustrated in Figure 1(a). Polaritons generated at each condensate node convert inherited potential energy into kinetic energy resulting in a radially (ballistically) expanding polariton fluid from an antenna like source [34, 35]. When two or more expanding condensates are brought together, interference effects are revealed implying phase synchronisation between the condensation centres and the emergence of a macroscopic order parameter [17, 22, 23, 35–37]. The striking homogeneity and large visibility of interference fringes in our optically-stabilised polariton lattices shown in Figure 1(a) indicate long-range coherence across the condensate systems.

The spatial coherence in a network (or lattice) of N polariton condensates generated under pulsed excitation is described by the integrated complex coherence factor (see Supplementary Section S2)

$$\tilde{\mu}_{ij} = \frac{\int \Gamma_{ij}(t)\mathrm{d}t}{\sqrt{\int \Gamma_{ii}(t)\mathrm{d}t \int \Gamma_{jj}(t)\mathrm{d}t}}, \quad i,j = 1,...,N. \tag{1}$$

Here, the correlation function $\Gamma_{ij}(t) = \left\langle \psi_i(t)^* \psi_j(t) \right\rangle$ denotes the mutual intensity of each pair of condensates averaged over many realisations (pulses) of the system, and $\psi_i(t)$ is the complex-valued amplitude of the ith condensate. While the modulus of the complex coherence factor $|\tilde{\mu}_{ij}| \leq 1$ is a normalised measure for the coherence between two condensate nodes its argument $\tilde{\theta}_{ij} = \arg(\tilde{\mu}_{ij})$ represents their average phase-difference.

A. Condensate density stabilisation

We utilise a reflective liquid-crystal phase-only spatial light modulator (SLM) to modulate the Gaussian excitation pump beam in the Fourier plane of the optical excitation system to generate desired excitation pump spot geometries at the focal plane of the microscope objective lens (see schematic in Figure 1(b)). Phase holograms are calculated using a modified version of the well-known Gerchberg-Saxton (GS) algorithm [38], in which the measured polariton photoluminescence (PL) of the condensate lattice feeds back into the closed-loop sequence (see Supplementary Section S3 for a full description). Iterative nonlinear adjustment of the excitation pump profile allows us to create macroscopic lattices of > 100 condensates with homogeneous condensate node density ($\leq 1\%$ relative standard deviation (RSD)) across the whole lattice.

In Figure 1(c) we compare the measured emission of all condensate nodes in a triangular lattice of 61 elements and lattice constant $a = 14.9$ μm when using 100 iterations of the conventional GS algorithm (blue squares) and the presented condensate density stabilisation method (red circles), respectively. Unavoidable effects such as sample disorder, finite accuracy of the GS algorithm, optical aberrations and missing translational invariance due the finite size of the lattice [39] all contribute to a broad distribution of effective gain for each condensate node and, thus, to a large spread $\approx 37\%$ (RSD) in the distribution of condensate emission powers for the case of no condensate density stabilisation. Active stabilisation of the lattice using the described closed-loop sequence allows us to compensate for these detrimental elements and yield a reduced spread $\approx 1\%$ (RSD), which is limited by experimental noise in the system.

The near-field (or real space) polariton photoluminescence (PL) measured at pump power $P = 1.2P_{\mathrm{thr}}$, where P_{thr} is the system's condensation threshold pump level, is shown in Figures 1(d) and (e) for both excitation schemes. The presence of interference fringes with large visibility in-between ballistically expanding condensates demonstrates mutual coherence between nearest neighbour condensates. However, the lack of homogeneity in the spatial distribution of interference fringes in Figure 1(d) for the case of no density stabilisation indicates a broad distribution of relative phase-difference θ_{ij} between nodes. This is further confirmed by detailed measurements of the integrated complex coherence factor $\tilde{\mu}_{ij}$ (see Supplementary Sections S4 and S5 for experimental details). In Figures 1(f) and (g) we plot magnitude $|\tilde{\mu}_{1j}|$ and phase $\tilde{\theta}_{1j}$ between the central condensate node 1 and each other condensate node j using false-color and pseudo-spins (black arrows). We find an enhanced and isotropic spatial decay of coherence $|\tilde{\mu}_{1j}|$ and larger homogeneity in relative phase-differences $\tilde{\theta}_{1j}$ for the density stabilised polariton lattice. The noticeable increase of phase-differences $\tilde{\theta}_{1j}$ - or analogous rotation of pseudo-spins - towards the edges of the lattice is an expected finite-size effect due to a flux of particles escaping the system [39]. In the ideal scenario of an infinite triangular lattice, with homogeneous condensate occupation numbers, one retrieves a homogeneous distribution of phase differences due to the system's translational invariance (see Supplementary Section S6).

The polariton condensate lattice is further probed by far-field (or reciprocal space) measurements in analogy to time-of-flight experiments in cold atom systems [19] (see Supplementary Section S4 for experimental methods). A zoom into the first Brillouin zones of the recorded far-field emission pattern is shown in Figures 2(a) and (b) for the two lattice realisations with and without node density stabilisation pumped at $P = 1.2P_{\mathrm{thr}}$. For comparison, we illustrate in Figure 2(c) the calculated far-field emission of 61 superimposed fully-coherent point-sources (wavefunctions) in triangular arrangement which shows good agreement with the emission pattern of the stabilised condensate lattice. We compare the width of the central far-field emission peak at $k = 0$ for the three cases shown in Figures 2(a-c) by plotting the corresponding extracted intensity profiles along $k_x = 0$ in Figure 2(d). The lobe of the calculated fully-coherent system (black line) represents the diffraction limited interference peak. We extract the central lobe's full-width-at-half-maximum (FWHM) for varying pump power P as shown in Figure 2(e) and find near-diffraction limited far-field emission for the density stabilised lattice (red dash-dotted line), i.e. a minimum width at $P = 1.17P_{\mathrm{thr}}$ which is only $\approx 13\%$ larger than the diffraction

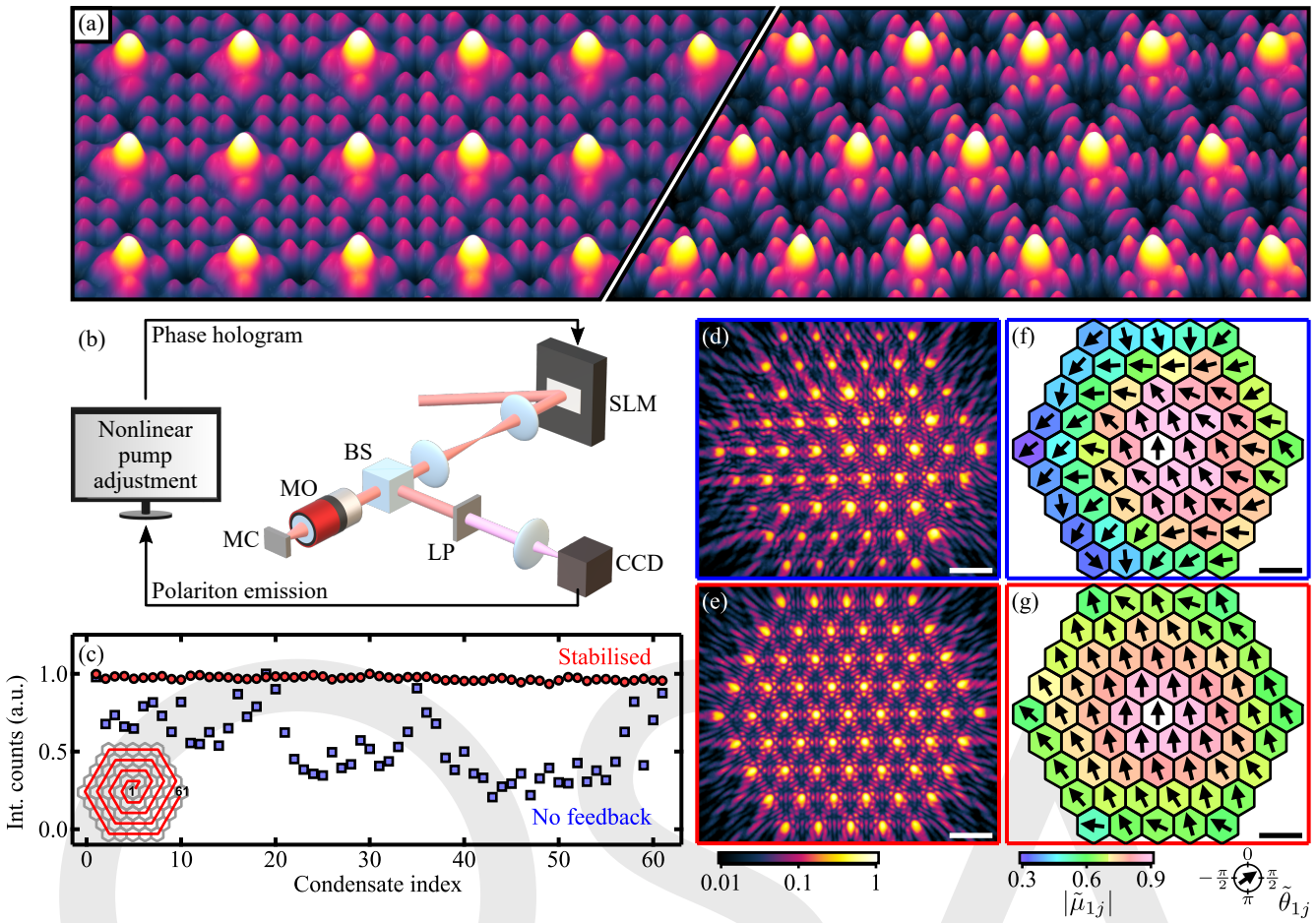

Fig. 1. Closed-loop density stabilisation in polariton lattices. (a) Three-dimensional views of the experimentally recorded condensate photoluminescence $|\Psi|^2$ of a stabilised polariton lattice in square (left) and triangular (right) configuration with lattice constant $a = 12.1$ μm and $a = 14.9$ μm, respectively. (b) Schematic of the feedback loop that iteratively analyses the emission and adjusts the pump profile to equalise the emission intensities of all condensate nodes. (c) Integrated emission of 61 condensate nodes at condensation threshold ($P = P_{\mathrm{thr}}$) in a triangular lattice configuration ($a = 14.9$ μm) without (blue squares) and with (red circles) density stabilisation. Inset depicts the condensate number indexing. (d,e) Recorded real-space photoluminescence and (f,g) measured complex coherence factor $\tilde{\mu}_{1j}$ between the central condensate node 1 and each other condensate node j without and with density stabilisation, respectively. False colourscale and pseudo-spins (black arrows) depict magnitude $|\tilde{\mu}_{1j}|$ and phase $\tilde{\theta}_{1j}$. Data shown in (a) and (d-g) are extracted at a total pump power $P = 1.2P_{\mathrm{thr}}$. Scale bars in (d-g) correspond to 20 μm. Plot elevation and false-color in (a) both represent the measured condensate density in logarithmic scale saturated below 0.8 % and 2.2 % for square and triangular lattice, respectively. Abbreviations in (b): SLM - spatial light modulator, BS - beam splitter, MO - microscope objective lens, MC - microcavity, LP - longpass filter, CCD - Charge-coupled device.

limit of a fully-coherent system (black horizontal line). Without active condensate density stabilisation (blue dashed line) the peak width increases to ≈ 47% at the same pump power. The observed broadening of the far-field emission peak in the physical system is a result of both reduced coherence $|\tilde{\mu}_{ij}|$ and non-homogeneous phase distribution $\tilde{\mu}_{ij}$. The system's pump-power dependencies are summarised in Supplementary Section S7.

B. Coherence vs. Dimensionality

In this section we begin by investigating the coherence between two ballistic polariton condensates. Previous studies of this system have revealed periodically alternating synchronisation patterns of in-phase ($\tilde{\theta}_{12} = 0$) and anti-phase ($\tilde{\theta}_{12} = \pi$) states with increasing condensate separation distance d_{12} [35, 36]. While there exist separation distances at which the emission of the coupled condensate system is not single-mode but exhibits two or more modes of both even and odd parity states [35, 36], in the following, we focus on single-mode realisations only. Under this condition the integrated complex coherence factor $\tilde{\mu}_{12}$ is a measure for the system's average coherence properties. In Supplementary Section S8 we detail on the time-resolved coherence build-up $\mu_{12}(t)$ of a polariton dyad.

Recorded near-field and far-field PL of two condensates separated by $d_{12} = 12.7$ μm and pumped equally at $P = 1.2P_{\mathrm{thr}}$ are shown in Figures 3(a) and (b). The interference patterns in both emission images reveal anti-phase synchronisation between the two condensates ($\tilde{\theta}_{12} = \pi$) due to the even number of interference fringes. Far-field emission consists predominantly of PL at large in-plane wavevector $k = 1.8$ μm^{-1} demonstrating the ballistic expansion of both condensates due to the strong repulsive interactions between polaritons and the pump-induced exciton reservoirs localised at each condensate center [40]. In

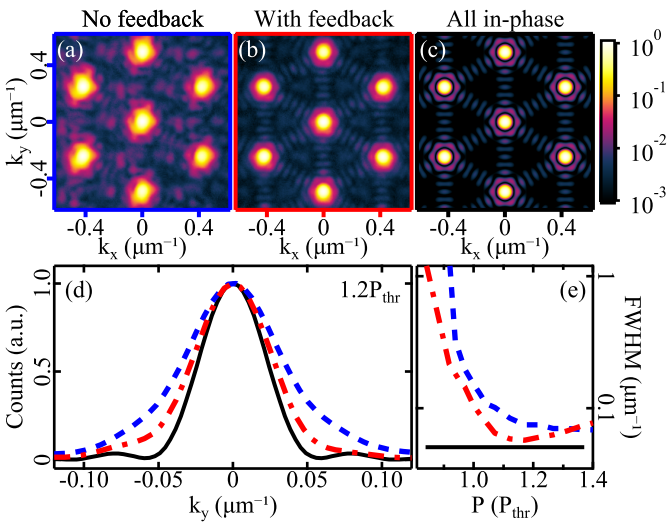

Fig. 2. Emission characteristics of a triangular polariton lattice in reciprocal space. First Brillouin zones of the far-field emission for a triangular polariton lattice of 61 condensates excited (a) without feedback, (b) with feedback and for (c) a calculated ideal system of 61 coherent phase-synchronised point sources. (d) Extracted profiles of the central Bragg peak along $k_x = 0$ for the far-field emission patterns shown in (a-c). (e) Extracted FWHM of the central Bragg-peak as a function of total excitation pump power. Data shown in (a,b,d) are recorded at pump power $P = 1.2P_{\mathrm{thr}}$.

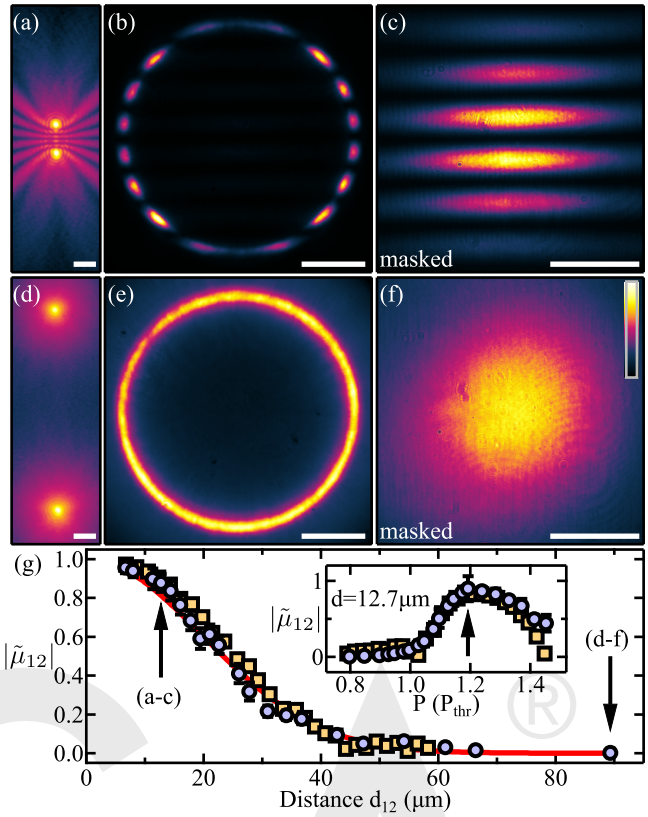

Fig. 3. Ballistic expansion, coupling and interference of two polariton condensates. Recorded (a,d) real-space and (b,e) far-field PL of two condensates with separation distances $d_{12} = 12.7$ μm and $d_{12} = 89.3$ μm. Corresponding far-field interference patterns after masking of the emission in real space to block all emission outside the 2 μm FWHM of each condensate node are shown in (c) and (f). (g) Distance dependence of the integrated complex coherence factor $|\tilde{\mu}_{12}|$, while keeping the excitation pump power constant at $P = 1.2P_{\mathrm{thr}}$, where P_{thr} is the measured threshold pump power at a distance of $d_{12} = 12.7$ μm. Blue circles correspond to experimental data and orange squares to GPE simulations. Red curve is a Gaussian fit (Equation (2)) to the experimental data points. Inset shows the pump power dependence of the coherence between two condensates separated at $d_{12} = 12.7$ μm. False color scale in (f) applies to (b,c,e,f) in linear scale and to (a,d) in logarithmic scale saturated below 10^{-4} of the maximum count rate. Scale bars in (a,d) and (b,c,e,f) correspond to 10 μm and 1 $\mu\mathrm{m}^{-1}$, respectively.

Figure 3(c) we show the recorded far-field interference pattern when spatially filtering the central 2 μm FWHM of each condensate. Analysis of this double hole interference pattern reveals a large coherence factor $|\tilde{\mu}_{12}| = 0.9$. Increasing the separation distance d_{12} while keeping the the pump power P constant leads to a decay of coherence $|\tilde{\mu}_{12}|$ between the two condensate centres such that at $d_{12} = 89.3$ μm no interference pattern can be found in near-field an far-field emission as shown in Figures 3(d-f).

The dependency of the measured coherence $|\tilde{\mu}_{12}|$ on the pump spot separation distance d_{12} is shown in Figure 3(g) as blue circles and is fitted with a Gaussian decay

$$|\tilde{\mu}_{12}(d_{12})| = \exp\left\{-\frac{\pi}{4}\left(\frac{d_{12}}{L_c}\right)^2\right\}. \quad (2)$$

The fit parameter $L_c = 24.9 \pm 0.4$ μm represents a measure for the length over which synchronisation of the two-condensate system is possible, and we denote it as the effective coherence length,

$$L_c = \int_0^{\infty} |\tilde{\mu}_{12}(x)| \mathrm{d}x.$$

We reproduce the experimentally measured decay of mutual coherence between two coupled polariton condensates through 2D numerical simulation using the generalised stochastic Gross-Pitaevskii equation (GPE) shown in Figure 3(g) as yellow squares (see methods in Supplementary Section S1). The dependency of coherence $|\tilde{\mu}_{12}|$ as a function of pump power P between two coupled condensates with separation distance $d_{12} = 12.7$ μm is depicted in the inset of Figure 3(g) for both experiment (blue circles) and numerical simulation (yellow squares). An increase of coherence between the two condensate nodes arising at condensation threshold is followed by a drop of $|\tilde{\mu}_{12}|$ for larger pump power $P > 1.2P_{\mathrm{thr}}$. This decrease in $|\tilde{\mu}_{12}|$ is largely attributed to the transition of the system into multi-mode operation [36] yielding reduced visibility in time-integrated measurements. We point out that the system realisations which are shown in the distance-dependence in Figure 3(g) exhibit single-mode emission only. The decrease in coherence with increasing separation distance is caused by the spatial decay of the wavefunction of ballistically expanding polariton condensates [35], i.e. a reduced coupling strength between the two condensate nodes. In Supplementary Section S9 we compare our results to a dyad under continuous wave excitation.

Next, we increase the number of condensates by investigating a linear chain of 11 equally spaced condensates with nearest-

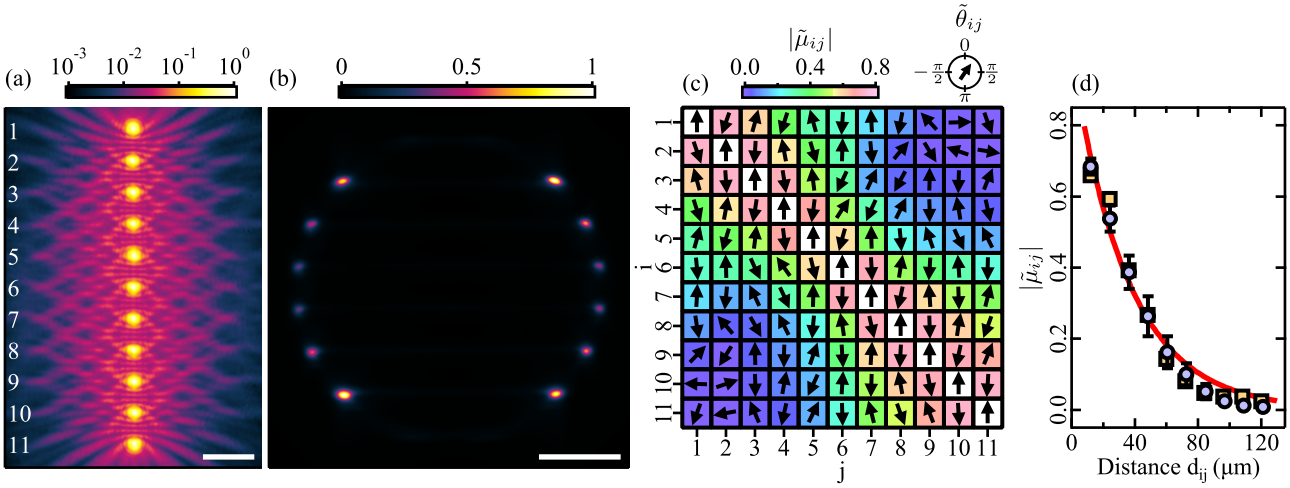

Fig. 4. Finite 1D lattice of ballistically coupled polariton condensates. Recorded (a) near-field and (b) far-field PL for 11 condensates arranged in a chain with lattice constant $a = 12.1$ μm. (c) Correlation matrix illustrating measured mutual coherence factor $|\tilde{\mu}_{ij}|$ and phase factor $\tilde{\theta}_{ij} = \arg(\tilde{\mu}_{ij})$ for each pair of condensates $i \neq j$. Condensate indexing is shown in (a). (d) Spatial decay of the averaged mutual coherence factors $|\tilde{\mu}_{ij}|$ from experiment (blue circles) and from GPE simulation (orange squares). Error bars represent the standard deviation of the set of coherence factor values for each separation distance d_{ij}. Red curve is an exponential fit to the experimental data points. The pump power is kept at $P = 1.2P_{\mathrm{thr}}$ for all data shown in (a-d). Scale bars in (a) and (b) correspond to 20 μm and 1 $\mu\mathrm{m}^{-1}$, respectively.

neighbours (NN) distance $a = 12.1$ μm. The resultant interference patterns in both real and reciprocal space shown in Figures 4(a) and (b) indicate anti-phase synchronisation, i.e. phase differences between any pair $\{i, j\}$ of condensates according to

$$\tilde{\theta}_{ij} = \pi \cdot (i - j) \mod \pi, \tag{3}$$

with condensate indexing shown in Figure 4(a). Such order can be said to be "antiferromagnetic". It differs from the in-phase synchronisation, or "ferromagnetic" order, shown for the triangular lattice in Fig. 1(g) due to the difference in lattice constant [17].

We measure and analyse the far-field interference between each pair of condensates $i \neq j$. Extracted magnitude $|\tilde{\mu}_{ij}|$ and phase $\tilde{\theta}_{ij}$ of the integrated complex coherence factor are illustrated in matrix form in Figure 4(c) with row and column indices i, j denoting the pair of condensates, where we make use of the hermiticity of the correlation matrix $\tilde{\mu}_{ij} = \tilde{\mu}^*_{ji}$. In agreement with Equation (3) we confirm anti-phase synchronisation between NNs (antiparallel pseudo-spins). For large condensate pair distances, $|i - j| \gg 1$, the coherence factor $\tilde{\mu}_{ij}$ decays in magnitude and its phase deviates from Equation (3) indicating loss of long-range antiferromagnetic order. In Figure 4(d) we show the decay of coherence $|\tilde{\mu}_{ij}|$ in the chain as a function of condensate spacing d_{ij} (i.e., lattice constant a is fixed). The data are fitted with a single exponential decay (red curve)

$$|\tilde{\mu}_{ij}| = \exp\left\{-d_{ij}/L_c\right\}, \tag{4}$$

which yields a coherence length $L_c = 35 \pm 1$ μm.

In a next step, we increase the system size to a 2D square lattice comprising 121 condensates with lattice constant $a = 12.1$ μm. The interference patterns in near-field and far-field PL which are shown in Figures 5(a) and (b) reveal anti-phase synchronisation in analogy to the 1D system in Figure 4. We measure $\tilde{\mu}_{1j}$ between the central condensate (index 1) and all other condensate nodes $j = 2, ..., 121$ plotted in Figure 5(c). The observed antiferromagnetic order ($\tilde{\mu}_{1j} \approx \pm 1$) reduces with distance from the centre seen from the pseudo-spin rotation towards the edges in Figure 5(c) due to flux of particles escaping the lattice. However, coherence $|\tilde{\mu}_{1j}|$ between the most central condensate and any other condensate of the lattice does not drop below 0.3 for separation distances as large as $d_{1j} = 86$ μm towards the corners of the lattice. The spatial decay of coherence $|\tilde{\mu}_{1j}|$ is shown in Figure 5(d) and fitted with an exponential function (Equation (4), red curve) with coherence length $L_c = 87 \pm 1$ μm.

To compare the obtained results, we summarise in Figure 6(a) the spatial decay of coherence for four different types of networks; two coupled condensates, 1D chain, and 2D square and triangular lattices. For the lattices the data points for different separation distances d_{ij} correspond to different pairs of condensate nodes $\{i, j\}$. For the polariton dyad the physical separation distance between the two condensate nodes is changed. In all cases the pump power was chosen such as to maximise the coherence $|\tilde{\mu}_{12}|$ between a pair of NNs in the system. In Figure 6(c) we illustrate the extracted (effective) coherence length L_c versus the average number of NNs in each system. It is apparent that the coherence length L_c is increasing for systems with larger connectivity which we explain in the following. Interestingly, the mutual coherence between NNs in the 1D chain ($d_{ij} = a$) is noticeably lower than in the other systems. Perhaps most surprisingly, the chain's coherence is lower than the dyad for small d_{ij} and then overtakes it around $d \gtrsim 25$ μm. The qualitative difference between the observed decay of coherence in the dyad (Gaussian) compared to the lattice systems (exponential) can possibly be attributed to the fact that the lattices are characterized by Bloch waves moving from unit cell to unit cell which can experience amplification from the pump spots. In the dyad, however, empty space separates the two condensates and the plane waves traveling between them decay quickly with increasing separation distance.

We attribute the origin of increased spatial coherence for

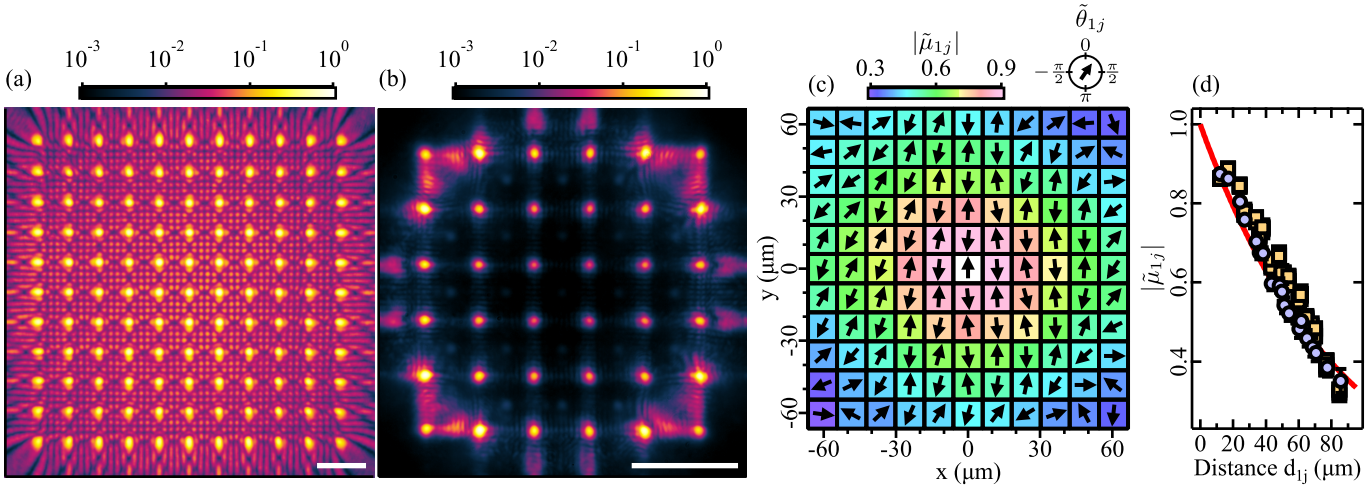

Fig. 5. Finite two-dimensional square lattice of ballistically coupled polariton condensates. Recorded (a) near-field and (b) far-field PL for 121 condensates arranged in a square lattice with lattice constant $a = 12.1$ μm. Spatial correlation map showing mutual coherence factor $|\tilde{\mu}_{1j}|$ and phase factor $\tilde{\theta}_{1j} = \arg(\tilde{\mu}_{1j})$ between the most central condensate (index 1) and each other condensate (index j). (d) Spatial decay of the averaged mutual coherence factors $|\tilde{\mu}_{1j}|$ from experiment (blue circles) and from GPE simulation (orange squares). Error bars represent the standard deviation of the set of coherence factor values for each separation distance d_{ij}. Red curve is an exponential fit to the experimental data points. The pump power is kept at $P = 1.2P_{\text{thr}}$ for all data shown in (a-d). Scale bars in (a) and (b) correspond to 20 μm and 1 μm^{-1}, respectively.

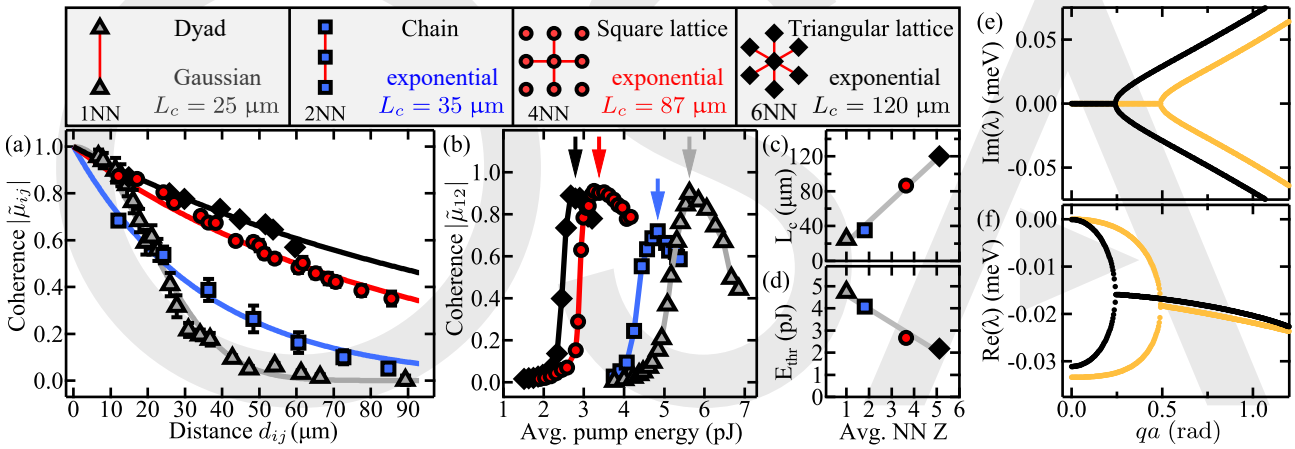

Fig. 6. Comparison of coherence between ballistically coupled polariton condensates in different networks presented in Figures 1, 3, 4 and 5. (a) Spatial decay of coherence for a two condensate system of varying size (grey triangles), a 1D chain (blue squares), a square lattice (red squares) and a triangular lattice (black diamonds). Curves represent Gaussian and exponential fits to the experimental data points. (b) Excitation pulse energy dependence of the mutual coherence factor $|\tilde{\mu}_{12}|$ between the central-most condensate (index 1) and one of its NNs (index 2) for the 1D and 2D periodic structures, and between two condensates at $d_{12} = 12.7$ μm for the case of a dyad. The pump powers used in (a) are marked with vertical arrows and are given by $P \approx 1.2P_{\text{thr}}$, where P_{thr} is the threshold pump power for each system, respectively. (c,d) Coherence length L_c and average excitation pulse energy E_{thr} per condensate node at threshold versus the average number of NNs Z. (e,f) Calculated Lyapunov exponents in $\Gamma \rightarrow X$ crystal momentum space (q-space) around the Γ-point ($qa = 0$) belonging to a square condensate lattice with small (high) particle numbers given by yellow (black) curves.

condensate networks with larger connectivity to their reduced population of reservoir excitons as we argue in the following. In Figure 6(b) we compare the dependence of coherence $|\tilde{\mu}_{12}|$ between a pair of NNs as a function of the average excitation pulse energy per condensate in each system. We observe a reduction of threshold pulse energy E_{thr} per condensate node for networks with larger connectivity (larger number of NNs), which is shown in Figure 6(d) and attributed to the increased gain given by ballistic exchange of particles between neighbouring nodes. A lower pump energy generates a smaller reservoir of excitons for each condensate node and since reservoir-condensate interactions play a dominant role in condensate dephasing [41], a lower threshold pump energy will generally result in increased coherence properties.

By discretising the system into a set of interacting condensates [35] one can show that threshold pump power and coherence length scale approximately linear with the number of condensate NNs. Let us consider the steady state (without

phase frustration) of frequency ν such that the discretised Gross-Pitaevskii equation can be written,

$$\nu\psi_n = \left[V + \frac{i}{2}\left(\frac{P}{n_s + |\psi_n|^2} - \gamma\right)\right]\psi_n + (\epsilon + i\kappa)\sum_{\langle nm\rangle}\psi_m, \quad (5)$$

Here, ψ_n describes the phase and amplitude of the nth with sum over NNs, the potential V describes blueshift coming from the condensate interactions with itself and its noncondensed particle background, P is the laser power, n_s is the condensate saturation density, and γ is the polariton lifetime. The non-Hermitian interaction between condensates is captured with ϵ and κ. The condensation threshold (the lasing mode) belongs to the mode with the lowest particle decay and its background reservoir of noncondensed particles responsible for dephasing is written,

$$n_x^{(\mathrm{thr})} = n_s - \frac{Z\kappa}{R}, \quad (6)$$

where Z is the number of NNs and R is the scattering rate of reservoir particles into the condensate. The density of the reservoir $n_x^{(\mathrm{thr})}$ is proportional to the amplitude of random fluctuations experienced by the condensate (see methods in Supplementary Section S1) and therefore its coherence properties will depend on the number of neighbours Z. The first order spatial correlation function can be written,

$$\mu_{nm} \propto \exp\left[-f_{\mathbf{k},\omega}(\mathbf{r}_{nm})\right], \quad (7)$$

where $\mathbf{r}_{nm}$ is the distance vector between condensates n and m and $f_{\mathbf{k},\omega}$ is the phase-phase correlation function which determines the condensate's long range coherence properties [42]. It is beyond the scope of this study to calculate $f_{\mathbf{k},\omega}$ given the complicated spatial density of the condensate. At the length scale of the experiment we observe an exponential decay of spatial correlations in all cases (except for the polariton dyad) shown in Figure 6(a) and therefore we will assume that $f_{\mathbf{k},\omega} = |\mathbf{r}_{nm}|/L_c$ holds. Assuming frequency independent noise processes the coherence length L_c becomes inversely proportional to the strength of the noise [29, 42] and one obtains,

$$L_c \propto \frac{1}{\gamma + Rn_s - Z\kappa} \simeq \frac{1}{\gamma + Rn_s}\left[1 + \frac{Z\kappa}{\gamma + Rn_s}\right]. \quad (8)$$

The expected linear dependencies of both threshold pump power $P_{\mathrm{thr}} \propto n_x^{(\mathrm{thr})}$ (Equation (6)) and coherence length L_c (Equation (8)) are both indicated as gray lines in Figures 6(c,d). We point out that similar results (increasing coherence with larger connectivity and dimensionality in networks of coupled elements) have been observed in other technological platform such as in arrays of coupled VCSELs [43, 44], micromechanical oscillator arrays [45] as well as for coupled fiber lasers [46].

It is instructive to investigate the condensate's dispersion of elementary excitations (fluctuations) which directly relates to the behaviour of space-time correlations in the system. These are also known as Lyapunov exponents in stability analysis and characterize the stability of stationary, orbital, and chaotic solutions of nonlinear differential equations [47]. For simplicity we will focus on the case of a 2D square lattice such as displayed in Figure 5 in a steady state (continuous wave excitation). For our calculation of the Lyapunov exponents we will assume that we are working in the the bulk of the condensate and therefore the system is taken to have discrete translational invariance. This allows us to apply Bloch's theorem to the standard Bogoliubov treatment and solve the Lyapunov exponents in the reduced Brillouin zone of the condensate-pump lattice (see Supplementary Section S10).

In Figures 6(e,f) we plot the Lyapunov exponents around the Γ-point of the reduced Brillouin zone for two different numbers of particles in the condensate. Yellow and black colored curves correspond to $N \approx 100$ and ≈ 800 particles in the condensate unit cell respectively for a lattice constant of $a = 12$ μm. The spontaneously broken gauge symmetry of the condensate results in a gapless spectrum $\lambda(0) = 0$ but possesses some qualitative differences to that of thermodynamic equilibrium condensates which possess a phonon-like dispersion $\mathrm{Im}(\lambda)$ at low momenta [48]. Instead, $\mathrm{Im}(\lambda)$ (which corresponds to oscillatory evolution of the fluctuations) shows a purely diffusive branch $\mathrm{Im}(\lambda) = 0$ at low momenta. This arises due to the open-ness, or the dissipative character, of our condensate which modifies the standard Bogoliubov dispersion of elementary excitations, leading to a bifurcation point separating diffusive and dispersive regimes [49] and smoothing the superfluid transition around the Landau critical velocity. It is a general result of open condensed systems and not exclusive to polaritons.

$\mathrm{Re}(\lambda)$ corresponds to the decay (growth) rate of fluctuations (excitations) when negative (positive) valued. In the top branch of the pitchfork displayed in Fig. 6(f), we observe that $\mathrm{Re}(\lambda)$ is more negative for small wavevectors as more particles are in the condensate (black curve). This is in agreement with our experiment where coherence increases with pump power (particle number grows and decay of fluctuations increases) up to the point where single-mode (stationary) behaviour is lost. Our results are similar to those obtained for spatially uniform systems [42, 49, 50] underlining that spatial details of the condensate structure are not relevant to long-wavelength fluctuations.

3. DISCUSSION

We have demonstrated that the coherence properties in lattices of polariton condensates are enhanced by balancing the condensate emission across the system using a closed-loop feedback scheme to adjust the excitation pump geometry. This scheme reduces the effects of optical aberrations in the experimental system, as well as counteracts mode localisation due to sample non-uniformities [51] and non-homogeneous gain distribution across the coupled condensate network. While actively controlling the condensate lattice uniformity we have accurately determined phase and coherence between any pairs of condensates in different types of networks ranging from two condensate-systems to 1D and 2D periodic structures. The dynamics and synchronisation of coupled non-linear elements is critically influenced by the underlying coupling topology [7]. Here, we have shown that an increase in connectivity, i.e. number of NNs, significantly reduces the operational pump power per node and increases the coherence length demonstrating a promising route to polaritonic devices with networks of many coupled condensates with potential application in simulators and optical based computation. The presented measurements and techniques provide a deeper understanding on the coherence properties of coupled light-matter wave fluids in low dimensional quantum systems, and qualify for other open (dissipative) networks such as laser arrays and photon condensate lattices. Furthermore, our analysis of the lattice condensate fluctuations reveals similar long-wavelength dispersions to those of uniform systems which are regarded as the ideal case from a theoretical point of view. This suggests access to fundamental long-wavelength physics belonging to

uniform systems by designing instead an extended condensate lattice.

FUNDING

Skoltech NGP Program (Skoltech-MIT joint project); UK's Engineering and Physical Sciences Research Council (grant EP/M025330/1 on Hybrid Polaritonics); RFBR projects No. 20-52-12026 (jointly with DFG) and No. 20-02-00919; CONACYT (Mexico) Grant No. 251808; PAPIIT-UNAM Grant No. IN106320.

DISCLOSURES

The authors declare no conflicts of interest.

Please see Supplement Document for methods and supporting content.

REFERENCES

1. A. Pikovsky, J. Kurths, M. Rosenblum, and J. Kurths, *Synchronization: a universal concept in nonlinear sciences*, vol. 12 (Cambridge university press, 2003).
2. S. H. Strogatz, D. M. Abrams, A. McRobie, B. Eckhardt, and E. Ott, "Crowd synchrony on the millennium bridge," Nature **438**, 43–44 (2005).
3. C. M. Gray, P. König, A. K. Engel, and W. Singer, "Oscillatory responses in cat visual cortex exhibit inter-columnar synchronization which reflects global stimulus properties," Nature **338**, 334–337 (1989).
4. K. B. Davis, M. O. Mewes, M. R. Andrews, N. J. van Druten, D. S. Durfee, D. M. Kurn, and W. Ketterle, "Bose-Einstein condensation in a gas of sodium atoms," Phys. Rev. Lett. **75**, 3969–3973 (1995).
5. M. Bennett, M. F. Schatz, H. Rockwood, and K. Wiesenfeld, "Huygens's clocks," Proc. Royal Soc. London. Ser. A: Math. Phys. Eng. Sci. **458**, 563–579 (2002).
6. M. C. Soriano, J. García-Ojalvo, C. R. Mirasso, and I. Fischer, "Complex photonics: Dynamics and applications of delay-coupled semiconductors lasers," Rev. Mod. Phys. **85**, 421–470 (2013).
7. D. J. Watts and S. H. Strogatz, "Collective dynamics of 'small-world' networks," Nature **393**, 440–442 (1998).
8. S. H. Strogatz, "Exploring complex networks," Nature **410**, 268–276 (2001).
9. A. E. Motter, S. A. Myers, M. Anghel, and T. Nishikawa, "Spontaneous synchrony in power-grid networks," Nat. Phys. **9**, 191–197 (2013).
10. M. Romera, P. Talatchian, S. Tsunegi, F. A. Araujo, V. Cros, P. Bortolotti, J. Trastoy, K. Yakushiji, A. Fukushima, H. Kubota *et al.*, "Vowel recognition with four coupled spin-torque nano-oscillators," Nature **563**, 230–234 (2018).
11. T.-Y. Kao, J. L. Reno, and Q. Hu, "Phase-locked laser arrays through global antenna mutual coupling," Nat. Photonics **10**, 541–546 (2016).
12. O. Morsch and M. Oberthaler, "Dynamics of Bose-Einstein condensates in optical lattices," Rev. Mod. Phys. **78**, 179–215 (2006).
13. J. Struck, C. Ölschläger, R. Le Targat, P. Soltan-Panahi, A. Eckardt, M. Lewenstein, P. Windpassinger, and K. Sengstock, "Quantum simulation of frustrated classical magnetism in triangular optical lattices," Science **333**, 996–999 (2011).
14. I. Bloch, J. Dalibard, and S. Nascimbène, "Quantum simulations with ultracold quantum gases," Nat. Phys. **8**, 267–276 (2012).
15. D. Dung, C. Kurtscheid, T. Damm, J. Schmitt, F. Vewinger, M. Weitz, and J. Klaers, "Variable potentials for thermalized light and coupled condensates," Nat. Photonics **11**, 565–569 (2017).
16. A. Amo and J. Bloch, "Exciton-polaritons in lattices: A non-linear photonic simulator," Comptes Rendus Physique **17**, 934–945 (2016).
17. N. G. Berloff, M. Silva, K. Kalinin, A. Askitopoulos, J. D. Töpfer, P. Cilibrizzi, W. Langbein, and P. G. Lagoudakis, "Realizing the classical XY Hamiltonian in polariton simulators," Nat. Mater. **16**, 1120–1126 (2017).
18. D. Ballarini, A. Gianfrate, R. Panico, A. Opala, S. Ghosh, L. Dominici, V. Ardizzone, M. De Giorgi, G. Lerario, G. Gigli, T. C. H. Liew, M. Matuszewski, and D. Sanvitto, "Polaritonic neuromorphic computing outperforms linear classifiers," Nano Lett. **20**, 3506–3512 (2020).
19. Z. Hadzibabic, P. Krüger, M. Cheneau, B. Battelier, and J. Dalibard, "Berezinskii-Kosterlitz-Thouless crossover in a trapped atomic gas," Nature **441**, 1118–1121 (2006).
20. J. Kasprzak, M. Richard, S. Kundermann, A. Baas, P. Jeambrun, J. M. J. Keeling, F. M. Marchetti, M. H. Szymanska, R. André, J. L. Staehli, V. Savona, P. B. Littlewood, B. Deveaud, and L. S. Dang, "Bose-Einstein condensation of exciton polaritons," Nature **443**, 409–414 (2006).
21. E. Wertz, L. Ferrier, D. D. Solnyshkov, R. Johne, D. Sanvitto, A. Lemaître, I. Sagnes, R. Grousson, A. V. Kavokin, P. Senellart, G. Malpuech, and J. Bloch, "Spontaneous formation and optical manipulation of extended polariton condensates," Nat. Phys. **6**, 860–864 (2010).
22. G. Tosi, G. Christmann, N. G. Berloff, P. Tsotsis, T. Gao, Z. Hatzopoulos, P. G. Savvidis, and J. J. Baumberg, "Sculpting oscillators with light within a nonlinear quantum fluid," Nat. Phys. **8**, 190–194 (2012).
23. P. Cristofolini, A. Dreismann, G. Christmann, G. Franchetti, N. G. Berloff, P. Tsotsis, Z. Hatzopoulos, P. G. Savvidis, and J. J. Baumberg, "Optical superfluid phase transitions and trapping of polariton condensates," Phys. Rev. Lett. **110**, 186403 (2013).
24. T. Gao, E. Estrecho, K. Bliokh, T. Liew, M. Fraser, S. Brodbeck, M. Kamp, C. Schneider, S. Höfling, Y. Yamamoto *et al.*, "Observation of non-hermitian degeneracies in a chaotic exciton-polariton billiard," Nature **526**, 554–558 (2015).
25. L. Pickup, H. Sigurdsson, J. Ruostekoski, and P. Lagoudakis, "Synthetic band-structure engineering in polariton crystals with non-Hermitian topological phases," Nat. communications **11**, 1–8 (2020).
26. H. Deng, G. S. Solomon, R. Hey, K. H. Ploog, and Y. Yamamoto, "Spatial coherence of a polariton condensate," Phys. Rev. Lett. **99**, 126403 (2007).
27. D. N. Krizhanovskii, K. G. Lagoudakis, M. Wouters, B. Pietka, R. A. Bradley, K. Guda, D. M. Whittaker, M. S. Skolnick, B. Deveaud-Plédran, M. Richard, R. André, and L. S. Dang, "Coexisting nonequilibrium condensates with long-range spatial coherence in semiconductor microcavities," Phys. Rev. B **80**, 045317 (2009).
28. F. Manni, K. G. Lagoudakis, B. Pietka, L. Fontanesi, M. Wouters, V. Savona, R. André, and B. Deveaud-Plédran, "Polariton condensation in a one-dimensional disordered potential," Phys. Rev. Lett. **106**, 176401 (2011).
29. G. Roumpos, M. Lohse, W. H. Nitsche, J. Keeling, M. H. Szymańska, P. B. Littlewood, A. Löffler, S. Höfling, L. Worschech, A. Forchel, and Y. Yamamoto, "Power-law decay of the spatial correlation function in exciton-polariton condensates," Proc. Natl. Acad. Sci. **109**, 6467–6472 (2012).
30. D. Caputo, D. Ballarini, G. Dagvadorj, C. Sánchez Muñoz, M. De Giorgi, L. Dominici, K. West, L. N. Pfeiffer, G. Gigli, F. P. Laussy, M. H. Szymańska, and D. Sanvitto, "Topological order and thermal equilibrium in polariton condensates," Nat. Mater. **17**, 145–151 (2018).
31. H. Ohadi, Y. del Valle-Inclan Redondo, A. J. Ramsay, Z. Hatzopoulos, T. C. H. Liew, P. R. Eastham, P. G. Savvidis, and J. J. Baumberg, "Synchronization crossover of polariton condensates in weakly disordered lattices," Phys. Rev. B **97**, 195109 (2018).
32. A. Askitopoulos, L. Pickup, S. Alyatkin, A. Zasedatelev, K. G. Lagoudakis, W. Langbein, and P. G. Lagoudakis, "Giant increase of temporal coherence in optically trapped polariton condensate," arXiv e-prints arXiv:1911.08981 (2019).
33. F. Baboux, D. D. Bernardis, V. Goblot, V. N. Gladilin, C. Gomez, E. Galopin, L. L. Gratiet, A. Lemaître, I. Sagnes, I. Carusotto, M. Wouters, A. Amo, and J. Bloch, "Unstable and stable regimes of polariton condensation," Optica **5**, 1163–1170 (2018).
34. M. Richard, J. Kasprzak, R. Romestain, R. André, and L. S. Dang, "Spontaneous coherent phase transition of polaritons in CdTe microcavities," Phys. Rev. Lett. **94**, 187401 (2005).
35. J. Töpfer, H. Sigurdsson, L. Pickup, and P. Lagoudakis, "Time-delay polaritonics," Commun. Phys. **3**, 1–8 (2020).
36. H. Ohadi, R. L. Gregory, T. Freegarde, Y. G. Rubo, A. V. Kavokin, N. G. Berloff, and P. G. Lagoudakis, "Nontrivial phase coupling in polariton multiplets," Phys. Rev. X **6**, 031032 (2016).
37. S. Alyatkin, J. D. Töpfer, A. Askitopoulos, H. Sigurdsson, and P. G.

Lagoudakis, "Optical control of couplings in polariton condensate lattices," Phys. Rev. Lett. **124**, 207402 (2020).
38. R. Gerchberg and W. Saxton, "A practical algorithm for the determination of phase from image and diffraction plane pictures," Optik **35**, 237–246 (1972).
39. K. P. Kalinin and N. G. Berloff, "Networks of non-equilibrium condensates for global optimization," New J. Phys. **20**, 113023 (2018).
40. M. Wouters, I. Carusotto, and C. Ciuti, "Spatial and spectral shape of inhomogeneous nonequilibrium exciton-polariton condensates," Phys. Rev. B **77**, 115340 (2008).
41. M. Wouters and V. Savona, "Stochastic classical field model for polariton condensates," Phys. Rev. B **79**, 165302 (2009).
42. M. H. Szymańska, J. Keeling, and P. B. Littlewood, "Nonequilibrium quantum condensation in an incoherently pumped dissipative system," Phys. Rev. Lett. **96**, 230602 (2006).
43. A. Golshani, H. Pier, E. Kapon, and M. Moser, "Photon mode localization in disordered arrays of vertical cavity surface emitting lasers," J. Appl. Phys. **85**, 2454–2456 (1999).
44. H. Pier, E. Kapon, and M. Moser, "Strain effects and phase transitions in photonic resonator crystals," Nature **407**, 880–883 (2000).
45. M. Zhang, S. Shah, J. Cardenas, and M. Lipson, "Synchronization and phase noise reduction in micromechanical oscillator arrays coupled through light," Phys. Rev. Lett. **115**, 163902 (2015).
46. M. Fridman, M. Nixon, N. Davidson, and A. A. Friesem, "Passive phase locking of 25 fiber lasers," Opt. Lett. **35**, 1434–1436 (2010).
47. T. S. Parker and L. Chua, *Practical numerical algorithms for chaotic systems* (Springer Science & Business Media, 2012).
48. L. Pitaevskii and S. Stringari, *Bose-Einstein condensation and superfluidity*, vol. 164 (Oxford University Press, 2016).
49. M. Wouters and I. Carusotto, "Excitations in a nonequilibrium Bose-Einstein condensate of exciton polaritons," Phys. Rev. Lett. **99**, 140402 (2007).
50. A. Chiocchetta and I. Carusotto, "Non-equilibrium quasi-condensates in reduced dimensions," EPL **102**, 67007 (2013).
51. H. Pier and E. Kapon, "Photon localization in lattices of coupled vertical-cavity surface-emitting lasers with dimensionalities between one and two," Opt. Lett. **22**, 546–548 (1997).